J. Fluid Mech. (2018), *vol.* 852, *pp.* 398–421.
doi:10.1017/jfm.2018.540

Capillary processes increase salt precipitation during CO_2 injection in saline formations

Helena L. Kelly[1] **and Simon A. Mathias**[1,†]

[1]Department of Earth Sciences, Durham University, Durham DH1 3LE, UK

(Received 11 January 2018; revised 11 April 2018; accepted 1 July 2018;
first published online 7 August 2018)

An important attraction of saline formations for CO_2 storage is that their high salinity renders their associated brine unlikely to be identified as a potential water resource in the future. However, high salinity can lead to dissolved salt precipitating around injection wells, resulting in loss of injectivity and well deterioration. Earlier numerical simulations have revealed that salt precipitation becomes more problematic at lower injection rates. This article presents a new similarity solution, which is used to study the relationship between capillary pressure and salt precipitation around CO_2 injection wells in saline formations. Mathematical analysis reveals that the process is strongly controlled by a dimensionless capillary number, which represents the ratio of the CO_2 injection rate to the product of the CO_2 mobility and air-entry pressure of the porous medium. Low injection rates lead to low capillary numbers, which in turn are found to lead to large volume fractions of precipitated salt around the injection well. For one example studied, reducing the CO_2 injection rate by 94 % led to a tenfold increase in the volume fraction of precipitated salt around the injection well.

Key words: capillary flows, condensation/evaporation, geophysical and geological flows

1. Introduction

An important aspect of many international CO_2 emissions reduction plans involves storing CO_2 within the pore space of brine-containing aquifers, often referred to as saline formations (Nordbotten & Celia 2006; MacMinn, Szulczewski & Juanes 2010). The reason for choosing saline formations as opposed to freshwater aquifers is the idea that brine is sufficiently saline that it is unlikely to be suitable for exploitation as a future water resource. However, the dissolved salt within the brine can lead to operational problems (Miri & Hellevang 2016).

When CO_2 is injected into a saline formation, there is a high interfacial area between the CO_2 and the brine. Consequently, there is dissolution of CO_2 into the brine and evaporation of the water into the CO_2-rich phase (Spycher, Pruess & Ennis-King 2003). Surrounding the injection well, a dry-out zone develops where the water in the brine is completely evaporated. A consequence of this evaporation is that the dissolved salt precipitates as a solid phase, leading to significant loss of permeability around the injection well. Ultimately, this process can lead to complete deterioration of the injection well (Miri & Hellevang 2016).

† Email address for correspondence: s.a.mathias@durham.ac.uk

A number of numerical modelling studies have been undertaken to investigate important controls on salt precipitation in the dry-out zone. Zeidouni, Pooladi-Darvish & Keith (2009) derived an analytical solution using method of characteristics (MOC) to estimate the volume fraction of precipitated salt in the dry-out zone (hereafter referred to as C_{30}) due to CO_2 injection in saline formations. They concluded that the distribution of precipitated salt was uniform within the dry-out zone.

An important limiting assumption was that there is a local pressure equilibrium between the CO_2-rich and aqueous phases. The difference between the pressures of a non-wetting and wetting phase (the CO_2-rich and aqueous phases, respectively, in this context) is referred to as the capillary pressure. Pruess & Muller (2009) explored the same problem using the numerical reservoir simulator, TOUGH2, with the CO_2 storage module, ECO2N (Pruess & Spycher 2007). When capillary pressure is set to zero, C_{30} is found to be insensitive to injection rate. However, when capillary pressure is accounted for, C_{30} is found to increase with reducing CO_2 injection rate.

A physical explanation is provided as follows (Pruess & Muller 2009): capillary pressure is significantly increased as the wetting saturation is reduced. This can lead to a reversing in the direction of the wetting pressure gradient, which in turn results in counter-current flow, whereby brine flows in the opposite direction to the injected CO_2. The counter-current flow provides additional brine to the dry-out zone leading to an increased availability of salt for precipitation. The counter-current flow rate is driven by phase saturation gradients. As the injection rate increases, the counter-current flow becomes less significant in comparison.

Kim *et al.* (2012) extended the work of Pruess & Muller (2009) by performing a wider sensitivity analysis. They found that the value of C_{30} was significantly increased for scenarios involving high permeability and low injection rates. Furthermore, contrary to Zeidouni *et al.* (2009), they found that C_{30} was non-uniform, with the highest values present at the edge of the dry-out zone. This localized increase in salt precipitation is attributed to the combined effects of gravity and capillary pressure driven counter-current flow.

Li, Tchelepi & Benson (2013) found that smoother capillary pressure curves lead to faster dissolution of CO_2 into the aqueous phase. This is presumably because smoother capillary pressure curves lead to more capillary diffusion of the CO_2-rich phase and hence greater interfacial area between the CO_2-rich phase and the aqueous phase.

The suite of numerical simulations described by Pruess & Muller (2009) and Kim *et al.* (2012) have provided significant insight into the processes that control salt precipitation during CO_2 injection in saline formations. However, probably due to the perceived computational expense of numerically simulating this problem to an adequate accuracy, a more widespread sensitivity analysis has not been undertaken to further understand this process.

Analytical solutions have been developed to better understand many other aspects of the CO_2 storage process. Nordbotten & Celia (2006) developed a similarity solution to study the propagation rate of a CO_2 plume and its associated dry-out zone during injection of CO_2 into a cylindrical saline formation. Hesse *et al.* (2007), Hesse, Orr & Tchelepi (2008) and MacMinn *et al.* (2010), MacMinn, Szulczewski & Juanes (2011) developed MOC solutions to study the migration of CO_2 plumes following the cessation of injection. Mathias *et al.* (2011*a*) extended the analytical solution of Nordbotten & Celia (2006) to estimate the resulting pressure buildup within an injection well. Mathias *et al.* (2011*b*) combined the work of Zeidouni *et al.* (2009) and Mathias *et al.* (2011*a*) to study the role of partial miscibility between the CO_2 and brine on pressure buildup. More recently, Mathias, McElwaine & Gluyas (2014)

derived a MOC solution to estimate the temperature distribution around a CO_2 injection in a depleted gas reservoir. There are many other such examples in the literature. However, all the analytical solutions presented to date revolve around the CO_2 transport problem reducing to a hyperbolic partial differential equation (PDE), such that MOC or some variant can be used for the solution procedure. The difficulty of accounting for capillary pressure is that this leads to a diffusive component within the equations, rendering MOC inadequate in this regard.

Unrelated to CO_2 storage, McWhorter & Sunada (1990) derived a similarity solution to look at two-phase immiscible flow around an injection well, which explicitly captures the counter-current flow associated with capillary pressure effects. In the past, their solution has not been commonly used due to difficulties with evaluating the necessary nonlinear multiple integrals associated with their equations (Fucik *et al.* 2007). However, more recently, Bjornara & Mathias (2013) have provided a more efficient evaluation procedure by re-casting the equations as a boundary value problem, which they then solve using a Chebyshev polynomial differentiation matrix (Weideman & Reddy 2000).

The objective of this study is to use the method of Bjornara & Mathias (2013) and extend the similarity solution of McWhorter & Sunada (1990) to account for partial miscibility of phases, so as to study the control of capillary pressure on salt precipitation during CO_2 injection in saline formations.

The outline of this article is as follows. First, a PDE to describe partially miscible three-phase flow is presented. This is then reduced to an ordinary differential equation (ODE) by application of a similarity transform. The resulting boundary value problem is solved using a Chebyshev polynomial differentiation matrix. The necessary equations are then presented to determine the volume fraction of precipitated salt in the dry-out zone. A set of verification examples are presented based on a gas-displacing-oil scenario, previously presented by Orr (2007). A CO_2-injection-in-a-saline-formation scenario is then presented, which is compared with simulation results from TOUGH2 for verification. Finally, a wider sensitivity analysis is conducted to better understand the main controls in this context.

2. Mathematical model

A homogenous, cylindrical and porous saline formation is invoked with a thickness of H [L] and an infinite radial extent. The pore space is initially fully saturated with a brine of uniform NaCl concentration. Pure CO_2 is injected at a constant rate of Q_0 [L^3T^{-1}] into the centre of the saline formation via a fully penetrating injection well of infinitesimally small radius. The permeability of the saline formation is horizontally isotropic. However, a necessary simplifying assumption is that the vertical permeability is significantly smaller than the horizontal permeability such that gravity effects can be neglected. In this way, during the injection phase, fluid flow can be treated as a one-dimensional radially symmetric process.

Now we will describe the material mixture that resides within the pore space. Consider a mixture of three components: $i = 1$, 2 and 3. Components 1 and 2 are mutually soluble and can reside within both a non-wetting fluid phase and a wetting fluid phase, denoted hereafter as $j = 1$ and 2, respectively. Component 3 can dissolve into phase 2 and precipitate to form a solid phase, denoted hereafter as $j = 3$. However, component 3 is assumed not to be able to reside in phase 1 and components 1 and 2 are assumed not to be able to reside in phase 3. In the context of a CO_2–H_2O–NaCl system, $i = 1$, 2 and 3 for CO_2, H_2O and NaCl, respectively. All components are

assumed to be incompressible and not to experience volume change on mixing, such that component densities can be treated as constant throughout.

The volume fraction of component i for the combined mixture, C_i [−], is defined by

$$C_i = \sum_{j=1}^{3} \sigma_{ij} S_j, \tag{2.1}$$

where σ_{ij} [−] is the volume fraction of component i in phase j and S_j [−] is the volume fraction of phase j for the combined mixture, often to referred to as the saturation of phase j.

With no additional assumptions, it can be said that

$$\sum_{i=1}^{3} C_i = \sum_{i=1}^{3} \sigma_{ij} = \sum_{j=1}^{3} S_j = 1 \tag{2.2}$$

and

$$\sigma_{ij} = \begin{cases} C_i, & C_1 \notin (c_{12}(1-S_3), c_{11}(1-S_3)), & i \in \{1,2\}, & j \in \{1,2\} \\ c_{ij}, & C_1 \in (c_{12}(1-S_3), c_{11}(1-S_3)), & i \in \{1,2\}, & j \in \{1,2\} \\ 0, & C_1 \in [0,1], & i \in \{1,2\}, & j = 3 \\ 0, & C_3 \in [0,1], & i = 3, & j = 1 \\ C_3/S_2, & C_3 \in [0, c_{32}S_2), & i = 3, & j = 2 \\ c_{32}, & C_3 \in [c_{32}S_2, 1], & i = 3, & j = 2 \\ 1, & C_3 \in [0,1], & i = 3, & j = 3, \end{cases} \tag{2.3}$$

where c_{ij} [−] is the constant equilibrium volume fraction of component i in phase j. It further follows that

$$S_1 = \begin{cases} 0, & C_1 \leqslant c_{12}(1-S_3) \\ \dfrac{C_1 - c_{12}(1-S_3)}{c_{11} - c_{12}}, & c_{12}(1-S_3) < C_1 < c_{11}(1-S_3) \\ 1 - S_3, & C_1 \geqslant c_{11}(1-S_3) \end{cases} \tag{2.4}$$

and

$$S_3 = \begin{cases} 0, & 0 \leqslant C_1 \leqslant 1, & C_3 < c_{32}S_2 \\ \dfrac{C_3 - c_{32}}{1 - c_{32}}, & C_1 \leqslant c_{12}(1-S_3), & C_3 \geqslant c_{32}S_2 \\ \dfrac{(c_{11}-c_{12})C_3 - (c_{11}-C_1)c_{32}}{(1-c_{32})c_{11} - c_{12}}, & c_{12}(1-S_3) < C_1 < c_{11}(1-S_3), & C_3 \geqslant c_{32}S_2 \\ C_3, & C_1 \geqslant c_{11}(1-S_3), & C_3 \geqslant c_{32}S_2. \end{cases} \tag{2.5}$$

Under the above set of assumptions, fluid flow is controlled by the following set of one-dimensional radially symmetric mass conservation equations

$$\phi \frac{\partial C_i}{\partial t} = -\frac{1}{r}\frac{\partial}{\partial r}\left(r \sum_{j=1}^{2} q_j \sigma_{ij} \right), \quad i \in \{1,2,3\}, \tag{2.6}$$

where ϕ [−] is the saline formation porosity, t [T] is time, r [L] is radial distance from the injection well and q_j [LT^{-1}] is the flow of phase j per unit area, which can be found from Darcy's law

$$q_j = -\frac{kk_{rj}}{\mu_j}\frac{\partial P_j}{\partial r}, \quad j \in \{1, 2\}, \tag{2.7}$$

where k [L^2] is the saline formation permeability and k_{rj} [−], μ_j [$\mathrm{ML}^{-1}\mathrm{T}^{-1}$] and P_j [$\mathrm{ML}^{-1}\mathrm{T}^{-2}$] are the relative permeability, dynamic viscosity and pressure of phase j, respectively.

A detailed discussion with regards to justification for the above set of assumptions is provided in § 4 below.

The difference between the non-wetting and wetting phase pressure is referred to as the capillary pressure, P_c [$\mathrm{ML}^{-1}\mathrm{T}^{-2}$], i.e.

$$P_c = P_1 - P_2. \tag{2.8}$$

Because the component densities are assumed to be constant, the system of equations is divergence free and

$$\sum_{j=1}^{2} q_j = \frac{Q_0}{2\pi Hr}. \tag{2.9}$$

Substituting (2.7) and (2.8) into (2.9), solving for the partial derivatives of P_j and then substituting these back into (2.7) leads to

$$q_j = \frac{Q_0 f_j}{2\pi Hr} + \frac{(-1)^j k k_{r1} f_2}{\mu_1}\frac{\partial P_c}{\partial r}, \tag{2.10}$$

where, with further consideration of (2.4),

$$f_j = \begin{cases} [1 + (-1)^j]/2, & C_1 \leqslant c_{12}(1 - S_3) \\ \dfrac{k_{rj}}{\mu_j}\left(\displaystyle\sum_{j=1}^{2}\frac{k_{rj}}{\mu_j}\right)^{-1}, & c_{12}(1 - S_3) < C_1 < c_{11}(1 - S_3) \\ [1 + (-1)^{j-1}]/2, & C_1 \geqslant c_{11}(1 - S_3). \end{cases} \tag{2.11}$$

Also note that there is no capillary pressure gradient when only one fluid phase is present, i.e.

$$\frac{\partial P_c}{\partial r} = 0, \quad C_1 \notin (c_{12}(1 - S_3), c_{11}(1 - S_3)). \tag{2.12}$$

Substituting (2.10) into (2.6), therefore leads to

$$\frac{\partial C_i}{\partial \tau} = -\frac{\partial F_i}{\partial \xi}, \tag{2.13}$$

where

$$F_i = \begin{cases} \sigma_{i2}, & C_1 \leqslant c_{12}(1 - S_3) \\ \displaystyle\sum_{j=1}^{2} f_j\sigma_{ij} + \left(\frac{k_{r1}f_2}{Ca}\sum_{j=1}^{2}(-1)^j\sigma_{ij}\right)\xi\frac{\partial \psi}{\partial \xi}, & c_{12}(1 - S_3) < C_1 < c_{11}(1 - S_3) \\ \sigma_{i1}, & C_1 \geqslant c_{11}(1 - S_3) \end{cases} \tag{2.14}$$

and

$$\tau = \frac{Q_0 t}{\pi \phi H r_e^2}, \tag{2.15}$$

$$\xi = \frac{r^2}{r_e^2}, \tag{2.16}$$

$$\psi = \frac{P_c}{P_{c0}}, \tag{2.17}$$

where r_e [L] is an arbitrary reference length, P_{c0} [$\mathrm{ML^{-1}T^{-2}}$] is a reference 'air-entry' pressure for the porous medium of concern and Ca [−] is a dimensionless constant often referred to as the capillary number, found from

$$Ca = \frac{Q_0 \mu_1}{4\pi H k P_{c0}}. \tag{2.18}$$

The capillary number represents the ratio of the CO_2 injection rate to the product of the CO_2 mobility and air-entry pressure of the porous medium. It compares the relative effect of the frictional resistance associated with fluid movement with the surface tension, which acts across the interface between the CO_2-rich phase and the aqueous phase. Small values of Ca imply that capillary processes are important.

With regards to the initial condition and boundary conditions, let C_{il} [−] represent a uniform initial value of C_i in the saline formation and C_{i0} [−] represent a constant boundary value of C_i at the injection well for $i \in \{1, 2, 3\}$.

2.1. *Writing capillary pressure in terms of* C_1

As CO_2 is injected into the saline formation, H_2O evaporates from the brine leaving NaCl behind as a precipitate in a dry-out zone that develops around the injection well. Following the commencement of CO_2 injection, there are therefore three distinct zones within the saline formation that should be considered (see figure 1): (i) The dry-out zone, which surrounds the injection well and contains only precipitated salt and CO_2 in the non-wetting fluid phase. (ii) The full mixture zone, which surrounds the dry-out zone and contains CO_2, H_2O and NaCl, distributed between the wetting and non-wetting fluid phases. (iii) The initial saline formation fluid zone, which surrounds the full mixture zone and contains only H_2O and NaCl in a wetting fluid phase.

Inspection of (2.13) and (2.14) reveals that the problem is hyperbolic for $C_1 \notin (c_{12}(1-S_3), c_{11}(1-S_3))$ and not hyperbolic for $C_1 \in (c_{12}(1-S_3), c_{11}(1-S_3))$, because of the $\partial\psi/\partial\xi$ term. For the CO_2 injection scenario described above, both Zones 1 and 3 are hyperbolic. In contrast, Zone 2 is not hyperbolic. The discontinuities that separate the three zones are shock waves, which must satisfy the Rankine–Hugoniot condition (e.g. Orr 2007).

Within Zone 2, the displacement of a wetting phase by a non-wetting phase represents a continuous drainage cycle such that ψ can be treated as a unique function of S_2. Furthermore, because $S_3 = 0$ and $S_2 = 1 - S_1$, it follows, from (2.4), that

$$S_2 = \begin{cases} 1, & C_1 \leqslant c_{12} \\ \dfrac{c_{11} - C_1}{c_{11} - c_{12}}, & c_{12} < C_1 < c_{11} \\ 0, & C_1 \geqslant c_{11} \end{cases} \tag{2.19}$$

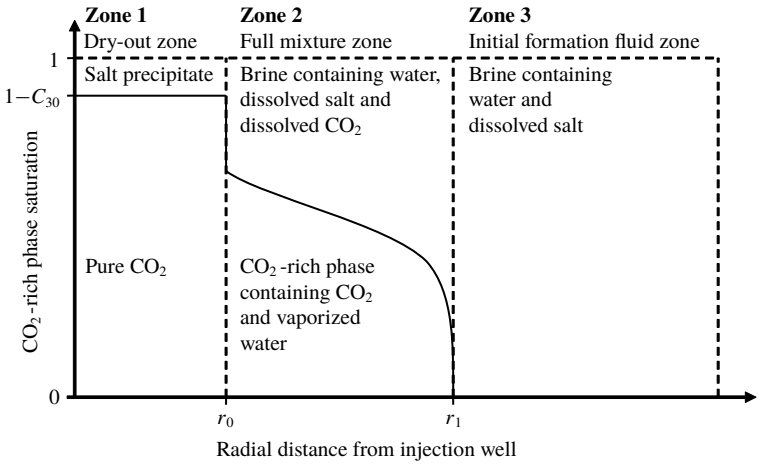

FIGURE 1. A schematic diagram illustrating the distribution of CO_2, water and salt around a CO_2 injection well in a saline formation.

and

$$\frac{\partial S_2}{\partial C_1} = \frac{1}{(c_{12} - c_{11})}, \quad C_1 \in (c_{12}, c_{11}) \tag{2.20}$$

such that it can be said that

$$\frac{\partial \psi}{\partial \xi} = \frac{1}{(c_{12} - c_{11})} \frac{\partial \psi}{\partial S_2} \frac{\partial C_1}{\partial \xi}. \tag{2.21}$$

In this way, equation (2.14) can be substantially simplified to get

$$F_i = \alpha_i - \beta_i \xi \frac{\partial C_1}{\partial \xi}, \tag{2.22}$$

where

$$\alpha_i = \begin{cases} C_i, & C_1 \notin (c_{12}, c_{11}), \quad i \in \{1, 2\} \\ \displaystyle\sum_{j=1}^{2} f_j c_{ij}, & C_1 \in (c_{12}, c_{11}), \quad i \in \{1, 2\} \\ f_2 \sigma_{32}, & C_1 \in [0, 1], \quad i = 3 \end{cases} \tag{2.23}$$

$$\beta_i = \begin{cases} 0, & C_1 \notin (c_{12}, c_{11}), \quad i \in \{1, 2, 3\} \\ G \displaystyle\sum_{j=1}^{2} (-1)^j c_{ij}, & C_1 \in (c_{12}, c_{11}), \quad i \in \{1, 2\} \\ G \sigma_{32}, & C_1 \in (c_{12}, c_{11}), \quad i = 3 \end{cases} \tag{2.24}$$

and

$$G = \frac{f_2 k_{r1}}{Ca(c_{11} - c_{12})} \frac{\partial \psi}{\partial S_2}. \tag{2.25}$$

When $Ca \to \infty$ and $\sigma_{32} = 0$, the above problem reduces to the hyperbolic problem solved by Orr (2007) using the MOC. When $c_{11} = 1$, $c_{12} = 0$ and $\sigma_{32} = 0$, the above problem reduces to the immiscible two-phase flow problem with capillary pressure, previously solved by McWhorter & Sunada (1990) and Bjornara & Mathias (2013). The G term in (2.25) is analogous to the G term in (16) of Bjornara & Mathias (2013).

2.2. *Relative permeability and capillary pressure functions*

Relative permeability is calculated from Corey curves but with relative permeability assumed to linearly increase with saturation to one beyond residual saturations:

$$k_{rj} = \begin{cases} 0, & S_j \leqslant S_{jc} \\ k_{rj0}\left(\dfrac{S_j - S_{jc}}{1 - S_{1c} - S_{2c}}\right)^{n_j}, & S_{jc} < S_j < 1 - S_{ic}, \quad i \neq j. \\ k_{rj0} + (1 - k_{rj0})\left(\dfrac{S_j - 1 + S_{ic}}{S_{ic}}\right), & S_j \geqslant 1 - S_{ic} \end{cases} \tag{2.26}$$

Dimensionless capillary pressure, ψ, is calculated using the empirical equation of van Genuchten (1980) in conjunction with, following Oostrom *et al.* (2016) and Zhang, Oostrom & White (2016), the dry-region extension of Webb (2000):

$$\psi = \begin{cases} (S_e^{-1/m} - 1)^{1/n}, & S_2 > S_{2m} \\ \psi_d \exp\left[\ln\left(\dfrac{\psi_m}{\psi_d}\right)\dfrac{S_2}{S_{2m}}\right], & S_2 \leqslant S_{2m}, \end{cases} \tag{2.27}$$

where S_e [−] is an effective saturation found from

$$S_e = \frac{S_2 - S_{2c}}{1 - S_{2c}} \tag{2.28}$$

and k_{rj0} [−], S_{jc} [−] and n_j [−] are the endpoint relative permeability, residual saturation and relative permeability exponent for phase j, respectively, m [−] and n [−] are empirical exponents associated with van Genuchten's function, $\psi_d = P_{cd}/P_{c0}$ [−] where P_{cd} [$\mathrm{ML^{-1}T^{-2}}$] is the capillary pressure at which 'oven-dry' conditions are said to have occurred (according to Webb (2000), this is taken to be 10^9 Pa) with

$$S_{2m} = (1 - S_{2c})S_{em} + S_{2c} \tag{2.29}$$

and

$$\psi_m = (S_{em}^{-1/m} - 1)^{1/n}, \tag{2.30}$$

where S_{em} [−] is a critical effective saturation at which the switch over between van Genuchten's function and Webb's extension take place, defined in the subsequent sub-section.

Differentiation of (2.27) with respect to S_2 leads to

$$\frac{\partial \psi}{\partial S_2} = \begin{cases} \dfrac{\psi}{(1 - S_{2c})mnS_e(S_e^{1/m} - 1)}, & S_2 > S_{2m} \\ \dfrac{\psi}{S_{2m}} \ln\left(\dfrac{\psi_m}{\psi_d}\right), & S_2 \leqslant S_{2m}. \end{cases} \tag{2.31}$$

The van Genuchten capillary pressure function has been widely used in many previous CO_2 injection studies (e.g. Pruess & Muller 2009; Kim *et al.* 2012; Mathias *et al.* 2013; Oostrom *et al.* 2016; Zhang *et al.* 2016). The Corey relative permeability functions have previously been useful in describing CO_2-brine relative permeability data from at least 25 different experiments from the international literature (Mathias *et al.* 2013).

2.3. *Determination of* S_{em}

Considering (2.31), Webb (2000) defines S_{em} as the effective saturation at which

$$\frac{\psi_m}{(1-S_{2c})mnS_{em}(S_{em}^{1/m}-1)} = \frac{\psi_m}{S_{2m}}\ln\left(\frac{\psi_m}{\psi_d}\right). \tag{2.32}$$

Substituting (2.30) and (2.29) into (2.32) and rearranging leads to

$$S_{em} = \frac{S_{em} + S_{2c}(1-S_{2c})^{-1}}{mn(S_{em}^{1/m}-1)\ln[(S_{em}^{-1/m}-1)^{1/n}\psi_d^{-1}]}, \tag{2.33}$$

which must be solved iteratively. Webb (2000) suggests that four to five iterations are sufficient. However, this will be strongly dependent on the initial estimate of S_{em0} applied.

For $S_{2c} > 0$, a good initial estimate of S_{em}, S_{em0}, can be obtained by assuming $S_{em0} \ll 1$ such that (2.33) reduces to

$$S_{em0} = \frac{S_{2c}(1-S_{2c})^{-1}}{\ln[S_{em0}\psi_d^{nm}]}, \tag{2.34}$$

which can be rearranged to get

$$W\exp(W) = z, \tag{2.35}$$

where

$$z = \frac{S_{2c}\psi_d^{nm}}{(1-S_{2c})} \tag{2.36}$$

and

$$W = \frac{S_{2c}}{(1-S_{2c})S_{em0}}. \tag{2.37}$$

Note that the functional inverse of $z(W)$ in (2.35), $W(z)$, is given by the Lambert W function. Furthermore, because z is always positive and real, $W(z) = W_0(z)$, otherwise referred to as the zero branch, which has the following asymptotic expansion (Corless *et al.* 1996)

$$W_0(z) = L_1 - L_2 + \frac{L_2}{L_1} + O\left(\left[\frac{L_2}{L_1}\right]^2\right), \tag{2.38}$$

where $L_2 = \ln L_1$ and $L_1 = \ln z$.

In this way, it can be said that

$$S_{em0} = \frac{S_{2c}}{(1-S_{2c})W_0(z)}, \tag{2.39}$$

where z is found from (2.36).

Iteration/S_{2c}	0.1	0.3	0.5	0.7
0	0.016496	0.054104	0.11525	0.2472
1	0.018951	0.061087	0.13012	0.29011
2	0.018927	0.061082	0.1305	0.29695
3	0.018927	0.061082	0.13051	0.29825
4	0.018927	0.061082	0.13051	0.29850
5	0.018927	0.061082	0.13051	0.29855
6	0.018927	0.061082	0.13051	0.29856
7	0.018927	0.061082	0.13051	0.29856

TABLE 1. Examples of the iterative calculation of S_{em} for different values of S_{2c} (as indicated in the top row) using (2.33) with $m = 0.5$, $P_{c0} = 19.6$ kPa and $P_{cd} = 10^9$ Pa. The initial guess, S_{em0}, is calculated using (2.39).

Examples of the iterative calculation of S_{em} from initial guesses obtained from (2.39) are presented in table 1. When $S_{2c} \leqslant 0.3$, it can be seen that convergence is achieved after just two iterations. When $S_{2c} = 0.5$, three iterations are required. When $S_{2c} = 0.7$, six iterations are required. The increase in the number of iterations required with increasing S_{2c} is due to reducing validity of the $S_{em} \ll 1$ assumption.

2.4. *Application of a similarity transform*

The partial differential equation in (2.13) can be reduced to an ordinary differential equation by application of the following similarity transform

$$\lambda = \frac{\xi}{\tau}. \tag{2.40}$$

Substituting (2.40) into (2.13) and (2.22) leads to

$$\frac{\mathrm{d}F_i}{\mathrm{d}C_i} = \lambda \tag{2.41}$$

and

$$F_i = \alpha_i - \beta_i \lambda \frac{\mathrm{d}C_1}{\mathrm{d}\lambda}. \tag{2.42}$$

Differentiating both sides of (2.41) with respect to C_i yields

$$\frac{\mathrm{d}^2 F_i}{\mathrm{d}C_i^2} = \frac{\mathrm{d}\lambda}{\mathrm{d}C_i}, \tag{2.43}$$

which on substitution into (2.42), along with (2.41), and rearranging leads to

$$\frac{\mathrm{d}^2 F_1}{\mathrm{d}C_1^2} + \frac{\beta_1}{(F_1 - \alpha_1)} \frac{\mathrm{d}F_1}{\mathrm{d}C_1} = 0. \tag{2.44}$$

In the event that the boundary and initial values of C_1, C_{10} and C_{1I}, respectively, are $\notin (c_{12}, c_{11})$, the boundary conditions for (2.44) must satisfy the Rankine–Hugoniot conditions (similar to Orr 2007, p. 75):

$$\frac{\mathrm{d}F_1}{\mathrm{d}C_1} = \frac{\alpha_{10} - F_1}{C_{10} - C_1}, \quad C_1 \geqslant c_{11}, \tag{2.45}$$

$$\frac{\mathrm{d}F_1}{\mathrm{d}C_1} = \frac{\alpha_{1I} - F_1}{C_{1I} - C_1}, \quad C_1 \leqslant c_{12}, \tag{2.46}$$

where α_{10} and α_{1I} represent the boundary and initial values of α_1 associated with C_{10} and C_{1I}, respectively. Alternatively, when C_{10} and C_{1I} are $\in(c_{12}, c_{11})$

$$\left.\begin{aligned} F_1 &= \alpha_{10}, \quad C_1 = C_{10}, \\ F_1 &= \alpha_{1I}, \quad C_1 = C_{1I}. \end{aligned}\right\} \tag{2.47}$$

An efficient way of expressing both (2.46) and (2.47) simultaneously is to state instead:

$$\left.\begin{aligned} (C_{10} - C_1)\frac{\mathrm{d}F_1}{\mathrm{d}C_1} + F_1 &= \alpha_{10}, \quad C_1 = \tilde{C}_{10}, \\ (C_{1I} - C_1)\frac{\mathrm{d}F_1}{\mathrm{d}C_1} + F_1 &= \alpha_{1I}, \quad C_1 = \tilde{C}_{1I}, \end{aligned}\right\} \tag{2.48}$$

where

$$\tilde{C}_{10} = H(C_{10} - c_{11})c_{11} + H(c_{11} - C_{10})C_{10}, \tag{2.49}$$

$$\tilde{C}_{1I} = H(c_{12} - C_{1I})c_{12} + H(C_{1I} - c_{12})C_{1I} \tag{2.50}$$

and $H(x)$ is a Heaviside function.

2.5. *Pseudospectral solution*

Following Bjornara & Mathias (2013), the boundary value problem described in the previous section is solved using a Chebyshev polynomial differentiation matrix, $\boldsymbol{D}$ (Weideman & Reddy 2000).

The coordinate space for the Chebyshev nodes is $x \in [-1, 1]$. However, the solution space for F_1 is $C_1 \in [\tilde{C}_{1I}, \tilde{C}_{10}]$. Therefore the Chebyshev nodes, $\boldsymbol{x}$, need to be mapped to the C_1 space by the following transform

$$C_1 = \frac{\tilde{C}_{10} + \tilde{C}_{1I}}{2} + \left(\frac{\tilde{C}_{10} - \tilde{C}_{1I}}{2}\right) x. \tag{2.51}$$

Consequently, it is necessary to introduce an appropriately transformed differentiation matrix, $\boldsymbol{E}$, where

$$\boldsymbol{E} = \frac{\mathrm{d}x}{\mathrm{d}C_1}\boldsymbol{D} \tag{2.52}$$

and from (2.51)

$$\frac{\mathrm{d}x}{\mathrm{d}C_1} = \frac{2}{\tilde{C}_{10} - \tilde{C}_{1I}}. \tag{2.53}$$

By applying the Chebyshev polynomial on the internal nodes and the Robin boundary conditions in (2.48) on the end nodes, equation (2.44) can be written in matrix form (similar to Piche & Kanniainen (2009) and Bjornara & Mathias (2013))

$$\boldsymbol{R}(\boldsymbol{F}) = \begin{bmatrix} \boldsymbol{E}^{(2)}_{2:N-1,:}\boldsymbol{F} + \boldsymbol{I}_{2:N-1,:}\mathrm{diag}\left[\dfrac{\beta_1}{F_1 - \alpha_1}\right]\boldsymbol{E}^{(1)}\boldsymbol{F} \\ (\boldsymbol{C}_N - C_{1I})\boldsymbol{E}^{(1)}_{N,:}\boldsymbol{F} - \boldsymbol{I}_{N,:}\boldsymbol{F} + \alpha_{1I} \\ (\boldsymbol{C}_1 - C_{10})\boldsymbol{E}^{(1)}_{1,:}\boldsymbol{F} - \boldsymbol{I}_{1,:}\boldsymbol{F} + \alpha_{10} \end{bmatrix}, \tag{2.54}$$

where $\boldsymbol{R}$ is the residual vector, $\boldsymbol{F}$ is the solution vector for the dependent variable F_1, $\boldsymbol{I}$ is an identity matrix, $\boldsymbol{C}$ is the vector containing the corresponding values of C_1 and N denotes the number of Chebyshev nodes to be solved for. The two last rows on the right-hand side of (2.54) impose the Robin boundary conditions. Also note that $\boldsymbol{E}^{(n)}$ can be obtained from $\boldsymbol{E}^n$.

The solution vector, $\boldsymbol{F}$, can be obtained by Newton iteration, whereby new iterations, $\boldsymbol{F}_{(i+1)}$, are obtained from

$$\boldsymbol{F}_{(i+1)} = \boldsymbol{F}_{(i)} - (\partial \boldsymbol{R}/\partial \boldsymbol{F}_{(i)})^{-1}\boldsymbol{R}(\boldsymbol{F}_{(i)}), \tag{2.55}$$

where $\partial \boldsymbol{R}/\partial \boldsymbol{F}$ is the Jacobian matrix defined as

$$\frac{\partial \boldsymbol{R}}{\partial \boldsymbol{F}} = \begin{bmatrix} \boldsymbol{E}^{(2)}_{2:N-1,:} + \boldsymbol{I}_{2:N-1,:}\mathrm{diag}\left[\dfrac{\beta_1}{F_1-\alpha_1}\right]\boldsymbol{E}^{(1)} - \boldsymbol{I}_{2:N-1,:}\mathrm{diag}\left[\mathrm{diag}\left[\dfrac{\beta_1}{(F_1-\alpha_1)^2}\right]\boldsymbol{E}^{(1)}\boldsymbol{F}\right] \\ (\boldsymbol{C}_N - C_{1I})\boldsymbol{E}^{(1)}_{N,:} - \boldsymbol{I}_{N,:} \\ (\boldsymbol{C}_1 - C_{10})\boldsymbol{E}^{(1)}_{1,:} - \boldsymbol{I}_{1,:} \end{bmatrix}. \tag{2.56}$$

Note that F_1 is bounded by α_1 and α_{10}. Therefore, a good initial guess is to set $F_1 = \alpha_{10}$. Following Bjornara & Mathias (2013), an additional correction step should be applied in the Newton iteration to force the solution, F_1, to be less than α_1. The Newton iteration loop is assumed to have converged when the mean absolute value of $\boldsymbol{R} \leqslant 10^{-9}$. With 100 Chebyshev nodes (i.e. $N = 100$), convergence is typically achieved with less than 200 iterations.

2.6. *Dealing with salt precipitation in the dry-out zone*

Now consider the case where pure CO_2 is injected into a porous medium (i.e. $\alpha_{10} = 1$) initially fully saturated with brine (i.e. $\alpha_{1I} = 0$). Let σ_{32} be the volume fraction of NaCl in phase 2 throughout the system. In this way, the volume fraction of H_2O in phase 2 prior to CO_2 injection is $(1 - \sigma_{32})$.

Let r_0 [L] and r_I [L] be the radial extents of the dry-out zone and injected CO_2 plume respectively. At any given time, the volume of H_2O evaporated by the CO_2, V_e [L^3], can be found from

$$V_e = 2\pi\phi H(1 - c_{11})\int_{r_0}^{r_I} rS_1 \,\mathrm{d}r. \tag{2.57}$$

The volume of salt precipitated in the dry-out zone, V_s [L^3], is found from

$$V_s = \frac{\sigma_{32}V_e}{1 - \sigma_{32}}. \tag{2.58}$$

The volume of the dry-out zone where the salt is precipitated, V_d [L^3], is found from

$$V_d = \pi\phi H r_0^2. \tag{2.59}$$

Another quantity of interest is the volume of CO_2 dissolved in the brine, V_c [L^3], which can be found from

$$V_c = 2\pi\phi H c_{12}\int_{r_0}^{r_I} r(1 - S_1) \,\mathrm{d}r. \tag{2.60}$$

Considering the definition of λ in (2.40) in conjunction with (2.15) and (2.16)

$$r_0^2 = \frac{Q_0 t \lambda_0}{\pi \phi H} \quad \text{and} \quad r_I^2 = \frac{Q_0 t \lambda_I}{\pi \phi H}, \tag{2.61}$$

where, recall (2.41) and (2.48), λ_0 and λ_I can be found from

$$\lambda_0 = \left.\frac{\mathrm{d}F_1}{\mathrm{d}C_1}\right|_{C_1=c_{11}} \quad \text{and} \quad \lambda_I = \left.\frac{\mathrm{d}F_1}{\mathrm{d}C_1}\right|_{C_1=c_{12}}. \tag{2.62}$$

In this way it can be understood that:

$$V_e = (1-c_{11})Q_0 t \int_{\lambda_0}^{\lambda_I} S_1 \,\mathrm{d}\lambda, \tag{2.63}$$

$$V_d = Q_0 t \lambda_0, \tag{2.64}$$

$$V_c = c_{12} Q_0 t \int_{\lambda_0}^{\lambda_I} (1-S_1) \,\mathrm{d}\lambda. \tag{2.65}$$

Noting that the rates at which V_s and V_d grow with time are constant it can also be understood that the volume fraction of precipitated salt, C_3, will be both uniform within the dry-out zone and constant with time. The value of C_3 within the dry-out zone, hereafter denoted as C_{30}, can be found from

$$C_{30} = \frac{(1-c_{11})\sigma_{32}}{(1-\sigma_{32})\lambda_0} \int_{\lambda_0}^{\lambda_I} S_1 \,\mathrm{d}\lambda. \tag{2.66}$$

Given that $C_{10} = 1 - C_{30}$, $C_{1I} = 0$, $\alpha_{10} = 1$ and $\alpha_{1I} = 0$, the boundary conditions in (2.48) reduce to

$$\left.\begin{aligned} \frac{\mathrm{d}F_1}{\mathrm{d}C_1} &= \frac{1-F_1}{1-C_{30}-c_{11}}, && C_1 = c_{11}, \\ \frac{\mathrm{d}F_1}{\mathrm{d}C_1} &= \frac{F_1}{c_{12}}, && C_1 = c_{12}. \end{aligned}\right\} \tag{2.67}$$

Values of C_{30} can be obtained iteratively by repeating the procedures outlined in § 2.5 with successive estimates of C_{30} obtained from (2.66). Using an initial guess of $C_{30} = 0$, this process is found to typically converge after less than 60 iterations. The integrals in (2.65) and (2.63) can be found by trapezoidal integration.

3. Sensitivity analysis

3.1. *Gas displacing oil*

As a first example, the gas-displacing-oil scenario previously presented in figures 4.13 and 4.15 of Orr (2007) is adopted. The parameters describing the scenario include $c_{11} = 0.95$, $c_{12} = 0.20$, $\sigma_{32} = 0$, $\mu_2/\mu_1 = 2$, $S_{1c} = 0.05$, $S_{2c} = 0.1$, $k_{r10} = k_{r20} = 1$ and $n_1 = n_2 = 2$. For the pseudospectral solution, a value for the van Genuchten (1980) parameter, m, is set to 0.5.

Plots of C_1 against $\mathrm{d}F_1/\mathrm{d}C_1$ (which, recall, is equal to ξ/τ) for this scenario are shown in figure 2. The different subplots show the effect of varying the boundary volume fraction, C_{10}, and the initial volume fraction, C_{1I}. The different colours relate to different assumed values of Ca. Increasing Ca can be thought of as analogous

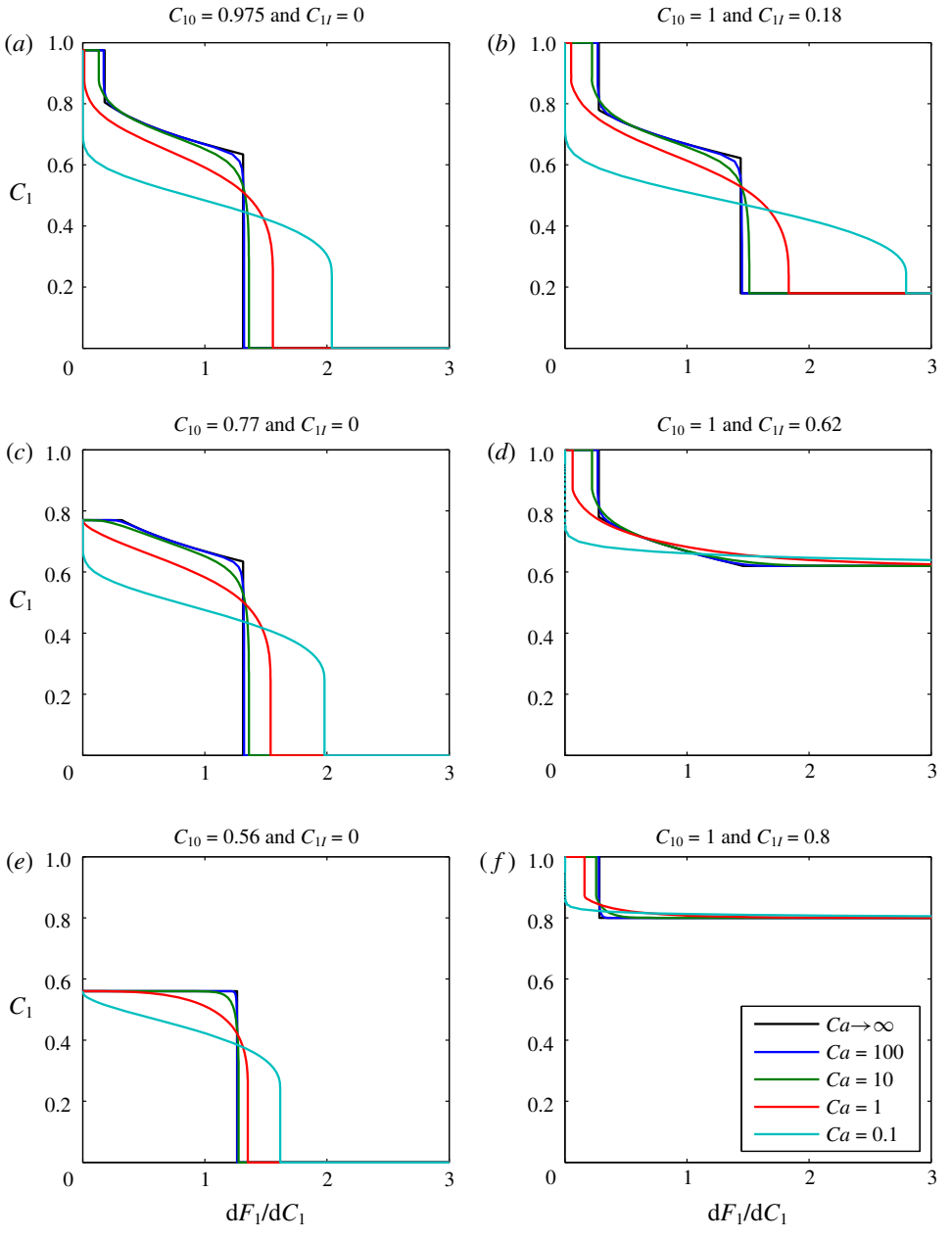

FIGURE 2. (Colour online) Sensitivity analysis based on gas-displacing-oil examples. The infinite *Ca* value curves were obtained from the method of characteristics solutions presented in figures 4.13 and 4.15 of Orr (2007). The finite *Ca* value curves were obtained using the pseudospectral solution documented in the current article.

to an increased injection rate. The $Ca \to \infty$ curves were obtained from the MOC solutions previously presented in figures 4.13 and 4.15 of Orr (2007). The finite *Ca* value solutions were obtained using the pseudospectral solution described above, with 100 Chebyshev nodes.

CO_2 injection rate,	15 kg s^{-1}
Porosity, ϕ	0.2
Initial pressure	10 MPa
Temperature	40 °C
Mass fraction of salt in brine, X_{32}	0.15
Critical gas saturation, S_{1c}	0.0
Residual water saturation, S_{2c}	0.5
Endpoint relative permeability for CO_2, k_{r10}	0.3
Endpoint relative permeability for brine, k_{r20}	1.0
Relative permeability exponents, n_1, n_2	3
Formation thickness, H	30 m
Permeability, k	10^{-13} m^2

TABLE 2. Relevant model parameters used for the CO_2 injection in saline formation scenario, previously presented by Mathias *et al.* (2013).

When $Ca = 100$, the pseudospectral solution is virtually identical to the infinite-Ca-MOC solutions. As Ca is decreased, the solution becomes more diffused. In figure 2(*a*,*b*,*d* and *f*), the infinity Ca results exhibit a trailing shock, which represents a dry-out zone where all the liquid oil has been evaporated by the gas. Of particular interest is that decreasing Ca leads to a reduction in the thickness of the dry-out zone, ultimately leading to its complete elimination.

3.2. *CO_2 injection in a saline formation*

Here the CO_2-injection-in-a-saline-formation scenario, previously presented by Mathias *et al.* (2013), is revisited. The example involves injecting pure CO_2 at a constant rate via a fully penetrating injection well at the centre of a cylindrical, homogenous and confined saline formation, initially fully saturated with brine. Relevant model parameters are presented in table 2. In this case, components 1, 2 and 3 are CO_2, H_2O and NaCl, respectively, and phases 1, 2 and 3 represent a CO_2-rich phase, an H_2O rich phase and precipitated salt, respectively.

The relevant fluid properties are obtained using equations of state (EOS) and empirical equations provided by Batzle & Wang (1992), Fenghour, Wakeham & Vesovic (1998), Spycher *et al.* (2003) and Spycher & Pruess (2005). Mathias *et al.* (2011*a*) found that when using analytical solutions in this context, to account for the relatively high compressibility of CO_2, it is important to use an estimate of the final pressure rather than the initial pressure for calculating the fluid properties relating to CO_2. Mathias *et al.* (2013) found that, for the scenario described in table 2, the well pressure increased by just over 5 MPa after 10 years. Therefore, for the current study, fluid properties are calculated using 15 MPa as opposed to 10 MPa.

The EOS of Spycher *et al.* (2003) and Spycher & Pruess (2005) provide equilibrium mole fractions as opposed to volume fractions. Pruess & Spycher (2007) show how mole fractions can be converted to mass fractions, x_{ij} [−], which can be converted to volume fractions, σ_{ij} [−], using (similar to Orr 2007, p. 19)

$$\sigma_{ij} = \frac{\rho_j x_{ij}}{\rho_{ij}}, \tag{3.1}$$

Depth (m)	1000	1500	2000
Pressure (MPa)	15	20	25
Temperature (°C)	40	60	80
Density of CO_2, ρ_{11} (kg m^{-3})	754	704	673
Density of H_2O, ρ_{22} (kg m^{-3})	998	992	984
Density of NaCl, ρ_{33} (kg m^{-3})	2160	2160	2160
Volume fraction of CO_2 in phase 1, c_{11} (−)	0.999	0.998	0.996
Volume fraction of CO_2 in phase 2, c_{12} (−)	0.041	0.043	0.045
Volume fraction of NaCl in phase 2, σ_{32} (−)	0.075	0.074	0.073
Dynamic viscosity of CO_2, μ_1 (cP)	0.064	0.057	0.054
Dynamic viscosity of brine, μ_2 (cP)	0.963	0.730	0.573

TABLE 3. Relevant model parameters used for the CO_2 injection in a saline formation scenario with a brine salinity of 150 ppt.

where ρ_{ij} [ML^{-3}] is the density of component i in phase j and ρ_j [ML^{-3}] is the composite phase density, which can be found from

$$\rho_j = \left(\sum_{i=1}^{N_c} \frac{x_{ij}}{\rho_{ij}} \right)^{-1}, \tag{3.2}$$

where N_c [−] is the number of components present. Because the pseudospectral solution above assumes component densities remain constant throughout, a decision is made that $\rho_{12} = \rho_{11}$, $\rho_{21} = \rho_{22}$ and $\rho_{32} = \rho_{33}$.

Table 3 shows how the various fluid properties vary with depth below sea level in this context. Depth is related to pressure by assuming hydrostatic conditions and then adding 5 MPa to allow for pressure induced by CO_2 injection. Depth is related to temperature by assuming a geothermal gradient of 40 °C km^{-1}. It can be seen that the volume fractions are largely unaffected by depth. However, the variation in brine viscosity and CO_2 density are more noticeable.

A comparison of results from the pseudospectral solution with those from the TOUGH2 simulation reported by Mathias *et al.* (2013) is shown in figure 3, alongside results for when $Ca \to \infty$, obtained using a MOC solution similar to that previously presented by Zeidouni *et al.* (2009) and Mathias *et al.* (2011*b*). Mathias *et al.* (2013) assumed $P_{c0} = 19.6$ kPa. Considering the other parameters in tables 2 and 3, this leads to a Ca value of 1.7. There is excellent correspondence between the MOC solution, the TOUGH2 results and the pseudospectral solution when $Ca = 1.7$.

A value of $P_{c0} = 19.6$ kPa is often used to describe saline formations in a CO_2 storage context (Rutqvist *et al.* 2007; Zhou *et al.* 2008; Mathias *et al.* 2013; Zhu *et al.* 2015, e.g.). Experimental analysis looking at four different sandstone reservoirs revealed a range of P_{c0} values from 1.3–7.1 kPa (Oostrom *et al.* 2016). Smaller values of P_{c0} imply larger pore diameters.

A hallmark of hyperbolic theory is that the problem can be reduced to a fundamental wave structure which constitutes the solution. In figure 3, it can be seen that such a wave structure is largely preserved, despite the inclusion of capillary diffusion. Furthermore, the wave velocity of the leading shock is virtually independent of Ca for the range of Ca values studied. However, decreasing Ca leads to a more diffused spreading wave caused by the increase in capillary diffusion, which in turn

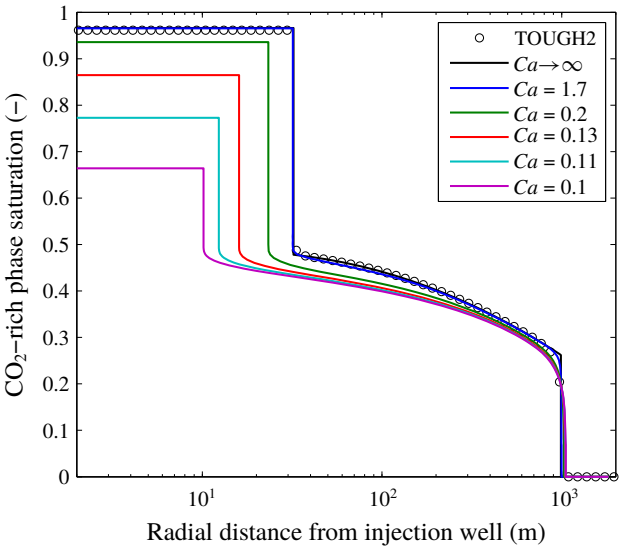

FIGURE 3. (Colour online) Plots of CO_2 saturation against radial distance after injecting 4.73 Mt of CO_2 whilst assuming a range of different capillary numbers, Ca. The TOUGH2 results are from the simulations previously presented by Mathias *et al.* (2013). Other associated model parameters are presented in table 2. The results for $Ca \to \infty$ were obtained using a method of characteristics solution, also presented by Mathias *et al.* (2013). The results for finite Ca values were obtained using the pseudospectral solution.

leads to a reduction in the wave velocity of the trailing shock, as also seen in figure 2(*a*). The decrease in steady-state CO_2 saturation in the dry-out zone is caused by an increase in the volume fraction of precipitated salt (recall that $C_{10} = 1 - C_{30}$).

For the scenarios depicted in figure 3, C_{30} is found to be insensitive to Ca for Ca values greater than or equal to 1.7. However for Ca values less than 1.7, the volume of the dry-out zone is significantly reduced and the volume fraction of precipitated salt is significantly increased. The value of C_{30} for $Ca = 0.2$ is almost double the value for $Ca = 1.7$. The value of C_{30} for $Ca = 0.1$ is around 10 times that of when $Ca = 1.7$. The $Ca = 1.7$ scenario described in table 2 assumes an injection rate of 15 kg s^{-1}. The results shown in figure 3 therefore suggest that reducing the injection rate down to 1.8 kg s^{-1} would lead to a doubling of the volume fraction of precipitated salt around the injection well. Furthermore, reducing the injection rate from 15 kg s^{-1} down to 0.9 kg s^{-1} would lead to an almost 10 times larger volume fraction of precipitated salt around the injection well.

For the hyperbolic case when $Ca \to \infty$, it is common to study plots of F_1 and C_1 (Orr 2007). Figure 4(*a*) shows plots of F_1 against C_1 for all the values of Ca presented in figure 3 along with a plot of α_1. The MOC solution (i.e. with $Ca \to \infty$), which sits almost exactly underneath the $Ca = 1.7$ line, intersects the α_1 line at tangents, which is symptomatic of satisfying the shock waves satisfying the Rankine–Hugoniot condition. To better visualize the results for finite Ca values, $(1 - F_1)$ is shown on a log scale in figure 4(*b*). Here it can be seen that the models approach a value of $F_1 = 1$ at different C_1 values depending on the volume fraction of precipitated salt. The volume fraction of precipitated salt increases with decreasing Ca. Figure 4(*c*) shows a close-up view of the trailing shocks on linear axes for further reference. For finite Ca values, the F_1

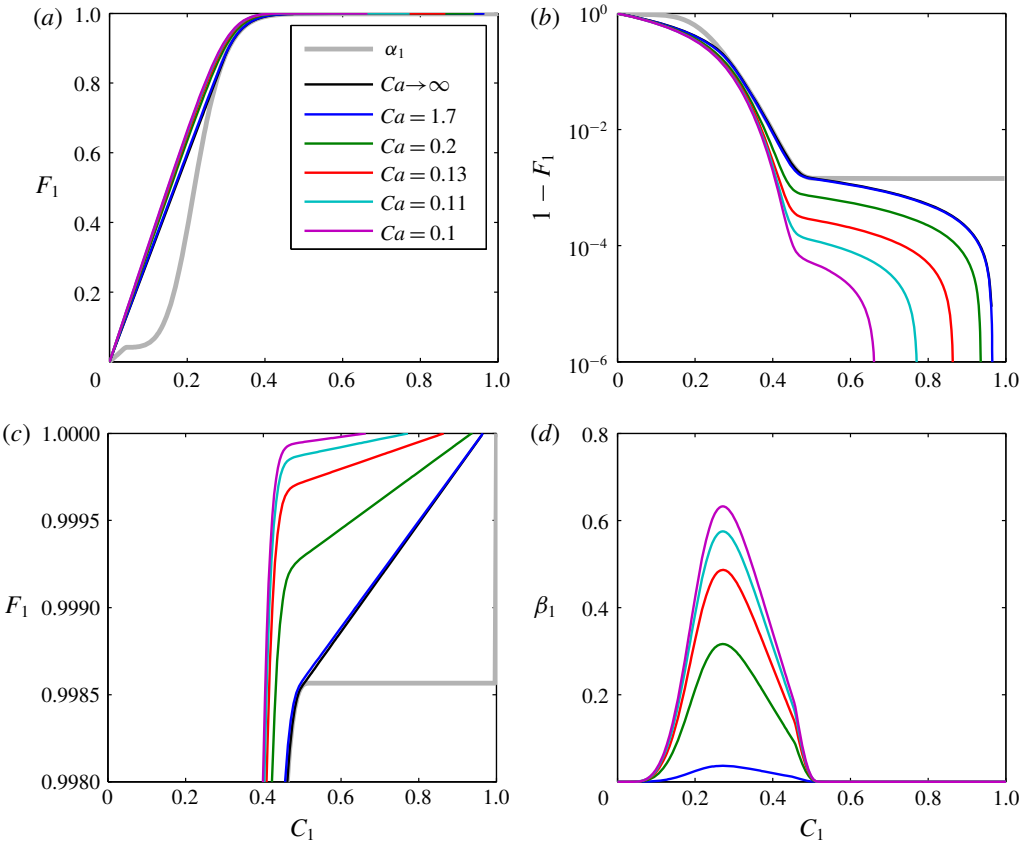

FIGURE 4. (Colour online) Plots of F_1, α_1 and β_1 against C_1 for the simulation results presented in figure 3.

lines never actually intersect the α_1 line except at where $C_1 = 0$. The reason for this is due to β_1, which is plotted in figure 4(*d*). The highest values of β_1 are at the centre of the two-phase region, $C_1 \in (c_{12}, c_{11})$. β_1 smoothly grades down to zero as it reaches the single-phase regions, $C_1 \notin (c_{12}, c_{11})$.

A further sensitivity analysis is presented in figure 5. The three depth scenarios presented in table 3 are applied with three different brine salinities. Figure 5(*a*) shows how the volume of the dry-out zone decreases with decreasing *Ca*. The size of the dry-out zone increases with increasing depth. In contrast, brine salinity has very little impact on dry-out zone volume.

Figure 5(*b*) shows the volume of the evaporated water also reduces with decreasing *Ca*. At first this seems surprising given that capillary pressure effects should bring more water into the dry-out zone. However, the effect of the capillary pressure is also to spread the CO_2 out further (see leading edge of CO_2 plumes in figure 3). As a consequence, more CO_2 is dissolved (see figure 5*c*). Consequently, less of the CO_2-rich phase is available for water from the brine to evaporate into. The volume of evaporated water increases with depth because the equilibrium volume fraction of water in the CO_2-rich phase increases with depth (see table 3). The volume of dissolved CO_2 is insensitive to depth but decreases with increasing brine salinity.

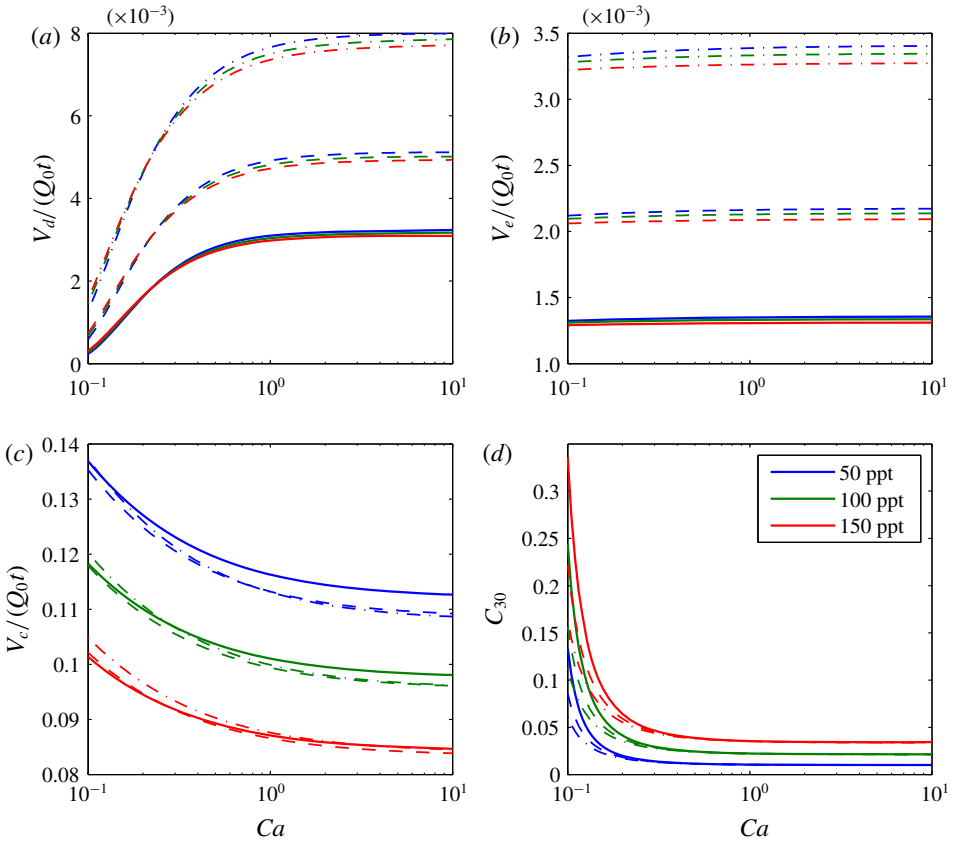

FIGURE 5. (Colour online) Sensitivity analysis based around the scenario presented in figure 3. The different colours relate to different brine salinities, as indicated in the legend. The solid lines, dashed lines and dash-dotted lines represent results obtained using fluid properties calculated assuming the saline formation exists at a depth of 1000 m, 1500 m and 2000 m, respectively (based on hydrostatic pressure conditions and a geothermal gradient of 40 °C km^{-1} as in table 3). (*a*) Shows plots of the ratio of dry-out zone volume (V_d) to injected CO_2 volume (Q_0t) against capillary number (Ca). (*b*) Shows plots of the ratio of volume of evaporated water (V_e) to Q_0t against Ca. (*c*) Shows plots of the ratio of volume of dissolved CO_2 (V_c) to Q_0t against Ca. (*d*) Shows plots of precipitated salt volume fraction in the dry-out zone (C_{30}) against Ca.

The latter is because the solubility limit of CO_2 in brine decreases substantially with increasing salinity (Spycher & Pruess 2005).

Figure 5(*d*) shows how volume fraction of precipitated salt in the dry-out zone, C_{30}, superlinearly increases with decreasing Ca. For $Ca > 0.25$, the quantity of precipitated salt is mostly controlled by brine salinity. However, for $Ca < 0.25$, depth plays an increasingly important role, with higher levels of salt precipitation in shallower formations. This is because the dry-out zone increases with depth, despite increasing water evaporation with depth. Figure 6 shows the same results as figure 5(*d*) but with C_{30} normalized by dividing by the salinity of the brine, X_{32}. Here it can be seen that C_{30} almost linearly scales with X_{32}.

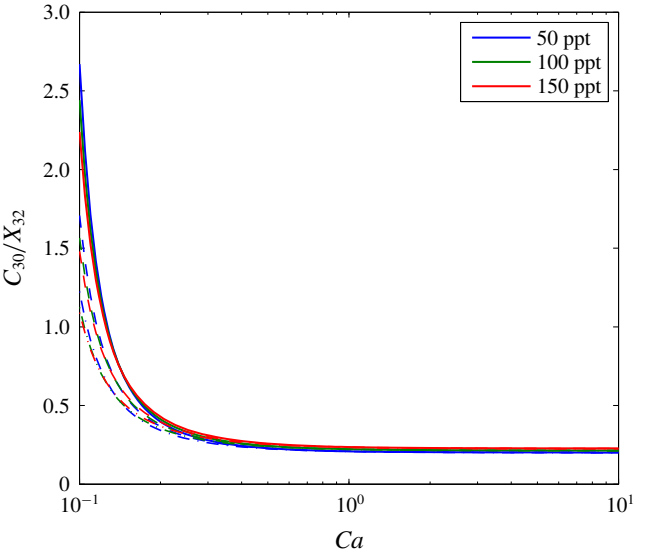

FIGURE 6. (Colour online) The same as figure 5(*d*) except that salt volume fraction, C_{30}, is divided by the salinity of the brine, X_{32}.

The volume fraction of precipitated salt is also strongly controlled by the relative permeability parameters, k_{rj0}, S_{jc} and n_j (Zhang *et al.* 2016). The analysis performed to provide figure 6 was repeated for the 1000 m depth scenario for each of the six groups of relative permeability parameters presented in table 4. These six parameter sets were selected from a database of 25 core experiments previously compiled by Mathias *et al.* (2013). The six cores were selected to provide a representative range of possible outcomes, given the wide variability generally observed in such data sets.

From figure 7 it can be seen that the high *Ca* values of C_{30} range from 0.019 to 0.044. Furthermore, the critical *Ca* value below which C_{30} superlinearly increases ranges from 0.025 to 10. Comparing these results with the parameter sets in table 4 it can be seen that when the relative permeability for brine is more linear, the value of C_{30} at high values of *Ca* tends to be lower. However, this linearity also leads to the superlinearly increasing of C_{30} with decreasing *Ca* to occur at a relatively low value of C_{30} (see for example Cardium no. 1 and Basal Cambrian). Exactly the opposite happens when the relative permeability for brine is highly nonlinear (see for example Paaratte and Tuscaloosa). This is probably due to counter-current flow of water being less efficient when relative permeability is highly nonlinear.

4. Discussion of key modelling assumptions

4.1. *Incompressible fluids*

Fluid densities are assumed to be independent of pressure. The compressibilities of H_2O and NaCl are commonly ignored. For pressures and temperatures associated with depleted gas reservoirs, the compressibility of CO_2 is very high and has a significant impact on fluid movement (Mathias *et al.* 2014). However, for CO_2 injection in saline formations, fluid pressures are expected to be hydrostatic or above. Under these conditions, providing a sensible reference pressure is used to determine the fluid properties of CO_2 (i.e. an estimate of pressure towards the end of the injection

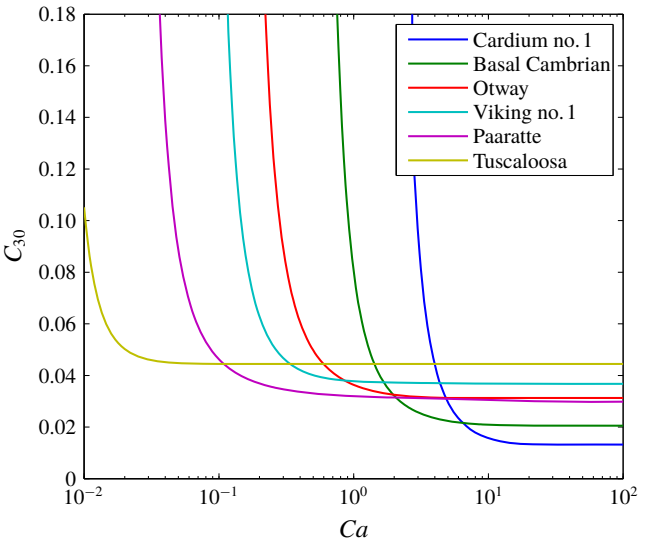

FIGURE 7. (Colour online) Plot of normalized precipitated salt volume fraction, C_{30}, against capillary number, Ca, using the 1000 m depth model scenario described in tables 2 and 3 in conjunction with the different relative permeability parameters given in table 4.

Unit	k_{r10}	S_{2c}	n_1	n_2
Cardium no. 1	0.526	0.197	1.7	1.3
Basal Cambrian	0.545	0.294	5.0	1.8
Otway	0.332	0.558	3.2	2.9
Viking no. 1	0.659	0.437	6.5	2.5
Paaratte	0.328	0.389	3.0	4.6
Tuscaloosa	0.077	0.703	3.2	4.7

TABLE 4. Relative permeability parameters for six different sandstone cores (after Mathias *et al.* 2013). Note that for each core $k_{r20} = 1$ and $S_{1c} = 0$. Data for Cardium no. 1, Basal Cambrian and Viking no. 1 were originally obtained by Bennion & Bachu (2008). Data for Otway were originally obtained by Perrin & Benson (2010). Data for Paaratte and Tuscaloosa were originally obtained by Krevor *et al.* (2012).

cycle), the compressibility of CO_2 has been found to have a negligible effect in this context (Mathias *et al.* 2011*a*,*b*).

4.2. *No volume change on mixing*

Component densities are assumed to be uniform across phases. In fact, the densities of CO_2 and H_2O are both higher in the aqueous phase as compared to in the CO_2-rich phase. For a wide range of different CO_2 injection scenarios, this volume change on mixing is found to lead to an increase in volumetric flow rate of around 0.05 % in Zone 2 and a decrease in volumetric flow rate of around 5 % in Zone 3 (see table 2 of Mathias *et al.* 2011*b*). See § 2.1 above for an explanation of the zone numbers.

With regards to NaCl, the density of precipitated NaCl, ρ_{33}, is 2160 kg m^{-3}. Using (3.2) in conjunction with the EOS for brine given by Batzle & Wang (1992), it can

be shown that the density of NaCl dissolved in brine, ρ_{32}, is around 2800 kg m^{-3}. In the above analysis we have set $\rho_{32} = \rho_{33}$ such that the model precipitates the correct volume of salt in the dry-out zone. The consequence is that the volume fractions of water and CO_2 in the brine are underestimated by around 2 %.

Figure 3 compares model results from TOUGH2 with those from the similarity solution. TOUGH2 properly incorporates fluid compressibility and volume change on mixing and there is negligible difference between the two models.

4.3. *Ignoring gravity effects*

As stated earlier, another important assumption is that the vertical permeability of the formation is sufficiently low that gravity effects can be ignored. Extreme changes in density and/or viscosity can lead to instabilities and fingering phenomena, which cannot be represented using one-dimensional models. Indeed, Kim *et al.* (2012) found that buoyancy driven flow, associated with the different densities of brine and CO_2, played an important part in controlling the spatial distribution of precipitated salt around an injection well. However, this was mostly after the cessation of injection. During the injection phase, gravity segregation within the dry-out zone was much less significant and no viscous fingering was observed.

Mathias *et al.* (2011*b*) presented a comparison of simulation results where gravity was accounted for and ignored using TOUGH2 and the MOC solution of Zeidouni *et al.* (2009), respectively. For a 100 m thick isotropic saline formation, gravity was found to have a strong effect on the leading edge of the CO_2 plume. However, gravity effects were found to be negligible on the dry-out zone development and the associated volume fraction of the precipitated salt. For a 50 m thick isotropic saline formation, gravity effects were found to be negligible throughout.

The dry-out zone is generally unaffected by gravity segregation due to the larger velocities situated close around the injection well, which are mostly horizontal due to the horizontal driving force provided by the injection well boundary (Mathias *et al.* 2011*b*). From the discussion above it is expected that gravity effects are unlikely to significantly affect the dry-out zone in the 30 m thick saline formations studied in this current article, at least for the lower capillary numbers studied. However, as the capillary numbers are increased, the horizontal injection velocities will become less significant and gravity will play a more important role. However, our analysis has shown that excessive salt precipitation can also develop in the absence of gravity effects due to the counter-current imbibition associated with capillary pressure.

5. Summary and conclusions

A new similarity solution has been presented to study the role of capillary pressure on salt precipitation during CO_2 injection in a saline formation. Dimensional analysis has revealed that the problem is largely controlled by a capillary number, $Ca = Q_0\mu_1/(4\pi HkP_{c0})$, where H [L] is the formation thickness, k [L^2] is permeability, P_{c0} [ML^{-1}T^{-2}] is an air-entry pressure associated with the porous medium, Q_0 [L^{3}T^{-1}] is the injection rate and μ_1 [ML^{-1}T^{-1}] is the dynamic viscosity of CO_2. The volume fraction of precipitated salt around the injection well, C_{30} [−], is found to superlinearly increase with decreasing Ca. Subsequent sensitivity analysis also reveals that C_{30} linearly scales with the salinity of brine. C_{30} is found to reduce with increasing storage depth. This latter point is largely attributed to the equilibrium volume fraction of water in the CO_2-rich phase increasing with depth. Relative permeability parameters are found to have a significant effect on the value of Ca

below which C_{30} superlinearly increases. For highly nonlinear relative permeabilities, C_{30} remains stable for much lower capillary numbers.

The new similarity solution represents a significant extension of the work of Zeidouni *et al.* (2009) by accounting for capillary pressure and an extension of the work of Bjornara & Mathias (2013) by accounting for radially symmetric flow, partial miscibility and salt precipitation.

In one scenario studied, reducing the CO_2 injection rate from 15 kg s^{-1} to 0.9 kg s^{-1} led to almost a 10 times larger volume fraction of precipitated salt. In the past, pressure buildup in injection wells has been widely perceived to increase monotonically with CO_2 injection rate. However, these results clearly demonstrate that as injection rate is decreased the volume fraction of precipitated salt around the injection well will significantly increase leading to potentially significant loss of injectivity. It follows that below a critical threshold, pressure buildup can be expected to increase with reducing injection rates as well. The similarity solution presented in this article can serve as a useful tool to determine the critical capillary number at which these effects are likely to take place.

Acknowledgement

This work was funded by the Crown Estate.

REFERENCES

BATZLE, M. & WANG, Z. 1992 Seismic properties of pore fluids. *Geophysics* **57**, 1396–1408.

BENNION, B. & BACHU, S. 2008 Drainage and imbibition relative permeability relationships for supercritical CO_2/brine and H_2S/brine systems in intergranular sandstone, carbonate, shale, and anhydrite rocks. *SPE Res. Eval. Engng* **11**, 487–496.

BJORNARA, T. I. & MATHIAS, S. A. 2013 A pseudospectral approach to the McWhorter and Sunada equation for two-phase flow in porous media with capillary pressure. *Comput. Geosci.* **17**, 889–897.

CORLESS, R. M., GONNET, G. H., HARE, D. E., JEFFREY, D. J. & KNUTH, D. E. 1996 On the LambertW function. *Adv. Comput. Maths* **5**, 329–359.

FENGHOUR, A., WAKEHAM, W. A. & VESOVIC, V. 1998 The viscosity of carbon dioxide. *J. Phys. Chem. Ref. Data* **27**, 31–44.

FUCIK, R., MIKYSKA, J., BENES, M. & ILLANGASEKARE, T. H. 2007 An improved semi-analytical solution for verification of numerical models of two-phase flow in porous media. *Vadose Zone J.* **6**, 93–104.

VAN GENUCHTEN, M. T. 1980 A closed-form equation for predicting the hydraulic conductivity of unsaturated soils. *Soil Sci. Soc. Am. J.* **44**, 892–898.

HESSE, M. A., ORR, F. M. & TCHELEPI, H. A. 2008 Gravity currents with residual trapping. *J. Fluid Mech.* **611**, 35–60.

HESSE, M. A., TCHELEPI, H. A., CANTWELL, B. J. & ORR, F. M. JR 2007 Gravity currents in horizontal porous layers: transition from early to late self-similarity. *J. Fluid Mech.* **577**, 363–383.

KIM, K. Y., HAN, W. S., OH, J., KIM, T. & KIM, J.-C. 2012 Characteristics of salt precipitation and the associated pressure build-up during CO_2 storage in saline aquifers. *Trans. Porous Med.* **92**, 397–418.

KREVOR, S., PINI, R., ZUO, L. & BENSON, S. M. 2012 Relative permeability and trapping of CO_2 and water in sandstone rocks at reservoir conditions. *Water Resour. Res.* **48**, W02532.

LI, B., TCHELEPI, H. A. & BENSON, S. M. 2013 Influence of capillary-pressure models on CO_2 solubility trapping. *Adv. Water Resour.* **62**, 488–498.

MACMINN, C. W., SZULCZEWSKI, M. L. & JUANES, R. 2010 CO_2 migration in saline aquifers. Part 1. Capillary trapping under slope and groundwater flow. *J. Fluid Mech.* **662**, 329–351.

MacMinn, C. W., Szulczewski, M. L. & Juanes, R. 2011 CO_2 migration in saline aquifers. Part 2. Capillary and solubility trapping. *J. Fluid Mech.* **688**, 321–351.

Mathias, S. A., Gluyas, J. G., Gonzlez Martnez de Miguel, G. J., Bryant, S. L. & Wilson, D. 2013 On relative permeability data uncertainty and CO_2 injectivity estimation for brine aquifers. *Intl J. Greenh. Gas Control* **12**, 200–212.

Mathias, S. A., Gluyas, J. G., Gonzlez Martnez de Miguel, G. J. & Hosseini, S. A. 2011 Role of partial miscibility on pressure buildup due to constant rate injection of CO_2 into closed and open brine aquifers. *Water Resour. Res.* **47**, W12525.

Mathias, S. A., Gonzalez Martinez de Miguel, G. J., Thatcher, K. E. & Zimmerman, R. W. 2009*a* Pressure buildup during CO_2 injection into a closed brine aquifer. *Trans. Porous Med.* **89**, 383–397.

Mathias, S. A., McElwaine, J. N. & Gluyas, J. G. 2014 Heat transport and pressure buildup during carbon dioxide injection into depleted gas reservoirs. *J. Fluid Mech.* **756**, 89–109.

McWhorter, D. B. & Sunada, D. K. 1990 Exact integral solutions for two-phase flow. *Water Resour. Res.* **26**, 399–413.

Miri, R. & Hellevang, H. 2016 Salt precipitation during CO_2 storage – a review. *Intl J. Greenh. Gas Control* **51**, 136–147.

Nordbotten, J. M. & Celia, M. A. 2006 Similarity solutions for fluid injection into confined aquifers. *J. Fluid Mech.* **561**, 307–327.

Oostrom, M., White, M. D., Porse, S. L., Krevor, S. C. M. & Mathias, S. A. 2016 Comparison of relative permeability–saturation–capillary pressure models for simulation of reservoir CO_2 injection. *Intl J. Greenh. Gas Control* **45**, 70–85.

Orr, F. M. Jr. 2007 *Theory of Gas Injection Processes*. Tie-Line Publications.

Perrin, J. C. & Benson, S. 2010 An experimental study on the influence of sub-core scale heterogeneities on CO_2 distribution in reservoir rocks. *Trans. Porous Med.* **82**, 93–109.

Piche, R. & Kanniainen, J. 2009 Matrix-based numerical modelling of financial differential equations. *Intl J. Math. Model Numer. Optim.* **1**, 88–100.

Pruess, K. & Muller, N. 2009 Formation dry-out from CO_2 injection into saline aquifers. 1. Effects of solids precipitation and their mitigation. *Water Resour. Res.* **45**, W03402.

Pruess, K. & Spycher, N. 2007 ECO2Na fluid property module for the TOUGH2 code for studies of CO_2 storage in saline aquifers. *Energy Convers. Manage.* **48**, 1761–1767.

Rutqvist, J., Birkholzer, J., Cappa, F. & Tsang, C. F. 2007 Estimating maximum sustainable injection pressure during geological sequestration of CO_2 using coupled fluid flow and geomechanical fault-slip analysis. *Energy Convers. Manage.* **48**, 1798–1807.

Spycher, N. & Pruess, K. 2005 CO_2–H_2O mixtures in the geological sequestration of CO_2. II. Partitioning in chloride brines at 12–100 °C and up to 600 bar. *Geochim. Cosmochim. Acta* **69**, 3309–3320.

Spycher, N., Pruess, K. & Ennis-King, J. 2003 CO_2–H_2O mixtures in the geological sequestration of CO_2. I. Assessment and calculation of mutual solubilities from 12 to 100 °C and up to 600 bar. *Geochim. Cosmochim. Acta* **67**, 3015–3031.

Webb, S. W. 2000 A simple extension of two-phase characteristic curves to include the dry region. *Water Resour. Res.* **36**, 1425–1430.

Weideman, J. A. C. & Reddy, S. C. 2000 A MATLAB differentiation matrix suite. *ACM Trans. Math. Softw.* **24**, 465–519.

Zeidouni, M., Pooladi-Darvish, M. & Keith, D. 2009 Analytical solution to evaluate salt precipitation during CO_2 injection in saline aquifers. *Intl J. Greenh. Gas Control* **3**, 600–611.

Zhang, Z. F., Oostrom, M. & White, M. D. 2016 Relative permeability for multiphase flow for oven-dry to full saturation conditions. *Intl J. Greenh. Gas Control* **49**, 259–266.

Zhou, Q., Birkholzer, J. T., Tsang, C. F. & Rutqvist, J. 2008 A method for quick assessment of CO_2 storage capacity in closed and semi-closed saline formations. *Intl J. Greenh. Gas Control* **2**, 626–639.

Zhu, Q., Zuo, D., Zhang, S., Zhang, Y., Wang, Y. & Wang, L. 2015 Simulation of geomechanical responses of reservoirs induced by CO_2 multilayer injection in the Shenhua CCS project, China. *Intl J. Greenh. Gas Control* **42**, 405–414.